Northumbria Research Link

Vision-based Spatial Damage Localization Method for Autonomous Robotic Laser Cladding Repair Processes

Habiba Zahir Imam[1], Hamdan Al-Musaibeli[1], Yufan Zheng[2], Pablo Martinez[3], Rafiq Ahmad*[1]

[1]Laboratory of Intelligent Manufacturing, Design and Automation (LIMDA), Department of Mechanical Engineering, University of Alberta, Edmonton, Canada

[2]School of Intelligent Manufacturing Ecosystem, Xi'an Jiaotong-Liverpool University, Suzhou, China

[3] Department of Mechanical and Construction Engineering, Northumbria University, Newcastle Upon Tyne, United Kingdom

*Corresponding author. Email: rafiq.ahmad@ualberta.ca

1   Abstract

Repair technologies have been considered as sustainable approaches due to their capability to restore value in a damaged component and bring it to like-new condition. However, in contrast to a manufacturing process benefiting from an automated environment, the automation level for repair and remanufacturing processes remains low. With the aim of moving the repair industry towards autonomy, this study proposes a novel repair framework. The developed methodology presents a vision-based Robotic Laser Cladding Repair Cell (RLCRC) that has two features: (a) an intelligent inspection system that uses a deep learning model to automatically detect the damaged region in an image; (b) employing computer vision-based calibration and 3D scanning techniques to precisely identify the geometries of damaged area. The repair of fixed bends is selected as the case study. The results obtained validate the efficacy of the proposed framework, enabling automatic damage detection and damaged volume extraction for worn fixed bends. Following the suggested framework, a time reduction of more than 63% is reported.

Keywords: repair systems; computer vision; autonomous manufacturing; deep learning.

1.   Introduction

A crucial strategy to achieve an environmentally conscious manufacturing sector is through remanufacturing. Remanufacturing is defined as a series of processes of repairing degraded components and bringing them to like-new condition, thus it can maintain the inherent energy of the virgin production. It is a well-established field that has garnered a lot of attention in research and industry due to its direct contribution to sustainable development by promoting product reuse [1,2].

Remanufacturing process involves disassembly, inspection, cleaning, recovery, rework, refurbish, and replacement. Specifically, different operations, e.g., additive operations (welding, spraying, laser cladding, etc.) and subtractive operations (machining, grinding, etc.), are implemented to recover a certain shape or specific geometry of damaged parts [3–6]. Among these operations, laser cladding (LC) has gathered a lot of interest for repairing and surface modification of mechanical components in the aerospace or oil and gas industries due to its ability to keep the heat-affected zone very shallow, reducing the risks of distortion, cracking and changing the metallurgy of the origin (base) material during the repairing/surface modification process [7]. This well-established industrial process works by focusing a high-power laser beam to generate a molten pool on the substrate along with continuously directing the material through a coaxial nozzle into that weld pool where it solidifies [8]. The scope of this presented research is LC-based repair technology.

Generally, the process involves identifying and locating damages on a part's surface and then depositing material to restore the original geometry by the LC technique [9]. However, repairing large volumes of worn components with the traditional repair process in industries is a monotonous and tedious task that, due to human dependence, can result in the process being time-consuming with a low throughput of parts and yielding inconsistent results. This issue is particularly relevant nowadays, as industries operate in a

rapidly changing environment due to factors like new technologies and global competition, which have created a necessity for industries to permanently transform their structures and technologies to survive in this dynamic setting [10].

As shown in Figure 1, a traditional LC-based repair process usually comprises six main preparatory steps: 1) the data acquisition to acquire data from the repaired part; 2) the defect detection and identification on the damaged part; 3) the reconstruction of the nominal model from the acquired data; 4) the registration of the nominal model with the damaged model; 5) the repair patch extraction using boolean operation on the nominal model and acquired model, and 6) the repair tool-path generation. This process relies heavily on human operators to acquire spatial information of the entire damaged component in the shape of three-dimensional (3D) point clouds by either using a structured light-based system or a laser triangulation-based scanner [11,12]. After obtaining a digital model of the worn part, the next step is to inspect the model and localize the damage. To localize the damage, either a nominal CAD model must be present, or the nominal model must be reconstructed from the damaged model. Registration is performed to align the damaged model with the nominal model by finding optimal point-to-point correspondences [13]. By comparing the registered models, the 3D geometry of the repair patch is extracted. This step is critical to the repair process because the repair volume's geometrical information is the basis on which a tool-path for deposition is generated [14]. By summarizing the traditional repairing process, the authors identify a few challenging problems that have not been addressed yet, listed as follows:

1. 3D scanning of the large volume part is time-consuming and result in dense point clouds that contain large amounts of data;

2. Reconstruction is computationally expensive and may cause some deviations between the reconstructed and the nominal model [15];

3. A robust registration of point clouds is challenging to obtain.

4. Due to tedious processes in traditional repairing processes ranging from data acquisition to tool-path generation, it is difficult to avoid manual operations.

These problems generate the gap to achieve an automated repairing process. Aprilia et al. [16] concluded an urgent need to develop algorithms for damage detection, localization, and tool-path generation that do not require human involvement.

| Data acquisition | Defect detection & identification | Reconstruction of the nominal model | Registration of the nominal model with the damaged model | Repair patch extraction | Tool-path generation |
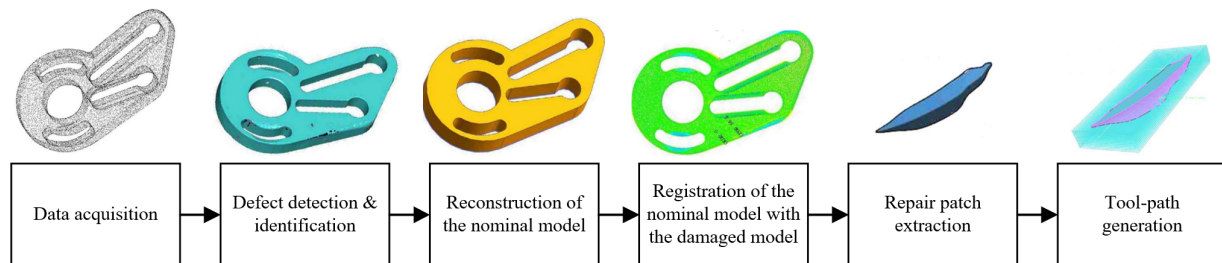
Figure 1. Flowchart outlining a traditional repairing process (adapted from [17]).

To move the repair industry towards autonomy, we introduce a novel damage quantification method that uses a camera to obtain a video feed of the worn component coupled with a laser triangulation sensor. This study aims to provide an overview of the intelligent robotic laser cladding repair cell while highlighting the important design choices made and the mathematical concepts used in the approach. As such, the system's calibration is covered, including the calculation of intrinsic and extrinsic matrixes and the validation of the camera model. Based on the validated calibration model, two case studies are carried out, and their respective error analyses are presented. This is the first autonomous repair pipeline based on

intelligent machine learning algorithms that incorporates a 2-dimensional (2D) camera and laser triangulation sensor to the best of the author's knowledge.

The rest of the paper is structured as follows. Section 2 reviews the current studies in damage inspection. Section 3 describes the proposed damage localization method. The results that validate the efficiency and accuracy of the proposed method are presented in Section 4. Finally, Section 5 summarizes this study and proposes some future works.

2. Literature Review

Damage or defect inspection is essential to enable autonomous or automatic repair. However, it has been the most challenging and tedious work, especially for dealing with minor defects or defects embedded in complex geometries. Researchers have devoted their efforts to solve this issue in two different directions, developing damage identification methods by collecting 3D point clouds or 2D images from the damaged component. Therefore, the relevant research results of these two categories related to the damage inspection methods are reviewed in this section.

2.1 Damage Inspection from Point Clouds

Advanced point cloud acquisition technologies such as coordinate measurement machines (CMM), triangulator systems, structured light systems, and stereo scanning systems have been widely employed to transform physical objects into digital objects [18]. However, point cloud information barely provides any more information than the 3D coordinates of scanned points. To identify the defective and non-defective areas, it is important to extract higher-level information from the point cloud. Surface segmentation methods have been widely implemented in the application of detection defects or damages from point cloud data. Point cloud segmentation methods can be divided into five categories: edge-based method, region-based method, attributes-based method, model-based method, and graph-based method [19].

Edge-based methods segments point cloud regions by identifying target points with rapid change in intensity [20,21]. In a region-based approach, neighboring points with a similar feature are integrated to isolate and distinguish regions with different features [22–24]. The attribute-based approach is based on clustering the attributes of the point cloud data [25–27]. Model-based method uses primitives for grouping surface fitting by the random sample consensus method. Graph-based method analyzes point clouds by a graph where each vertex corresponds to a point, and an edge links specific pairs of neighboring points. Recently, researchers have implemented these general surface segmentation methods to detect defects from point cloud data. Hitchcox and Zhao proposed a 'random walk' point cloud segmentation method to segment surface defects directly from unorganized 3D point clouds of aerospace surfaces [28]. Jovančević et al. introduced a 3D point cloud analysis based on the surface normal and curvature for detecting defects on exterior airplane's surfaces [29]. Since the point clouds are not smoothly continuous with the defective and non-defective area boundary, Gaussian curvatures analysis can reveal the discontinuity of two surface patches [17,30].

In addition to segmentation methods, comparing the reference point cloud and defective point cloud is an alternative approach to localize and characterize defective patches. Zheng et al. introduces an algorithm to compare the damaged and nominal parts through point clouds to extract the additive repair and subtractive repair patches [31]. Li et al. designed a fine registration method based on a modified iterative closet point (ICP) algorithm to identify the difference between defective part and nominal part [17]. Similarly, Zhang et al. proposes an automated damage detection method for jet engine blade repair, though comparing the overlapping area of nominal and damaged blades [12]. However, these methods are sometimes not feasible in practice because nominal models are not always available due to confidentiality issues [30]. 3D point cloud-based damage detection technology is also widely used in other fields, such as civil and factory facilities. Kashani & Graettinger introduced a cluster-based feature segmentation method

for light detection and ranging (LiDAR) point cloud for building roof damage detection [32]. Shinozaki et al. developed an automatic detection method to find scaffolding on furnace walls and wear from large-scale point clouds [33].

2.2 Damage Inspection from Images

An alternative damage inspection method is based on the analysis of images of damaged parts. Image-based damage inspection methods are classified into feature-based methods, template matching methods, and deep learning-based methods. Feature-based methods identify defects by a designed expert system that extracts certain properties of images, including colors, shapes, and/or textures. Zeng et al. [34] propose a light and shadow feature construction algorithm to automate the non-destructive testing for weld defect. Iglesia et al. [35] introduce an automated inspection system for identifying defects in slate slabs based on feature extraction. For feature-based defect detection methods, the quality of the features strongly depends on the experience of the system designer. In addition, the designed feature extractor is limited by the application scenario, which means that if the application scenario changes, the designed feature extractor may not be applicable anymore [36].

As an alternative method for damage detection from images, the template matching method identifies defects by matching the images of defect-free reference and the defective part. Tsai and Lin [37] introduce a fast normalized cross-correlation method to identify integrated circuit defects. Later, an improved template-matching method is developed to search for a template position by genetic algorithm [38]. Kong et al. [39] propose a unified framework for defect detection for industrial products with planar features based on the template matching method through a geometric alignment between the template and test images. The template matching-based approach has demonstrated effectiveness in detecting defects because of the prior knowledge of the template image. However, such methods have inherent weaknesses in defect detection in the remanufacturing/repair context due to the lack of template images.

In recent years, convolutional neural networks (CNN) have made substantial advances in the field of object detection and classification. Several researchers have implemented this algorithm in the defect detection problem, benefiting from this effective approach. Masci et al. [40] present a max-pooling CNN method to recognize and classify seven kinds of different steel defects. Wang et al. introduce a deep learning-based method to realize fast product inspection with guaranteed accuracy [36]. The method consists of three steps: Gaussian filtering, background removal based on Hough transform, and feature extraction by a deep neural network. A mask region-based CNN (Mask R-CNN) algorithm [41], a combined method to achieve object detection and instance segmentation, has been implemented for the inspection of casting defects from x-ray images [42]. Following that pattern, Zhang et al. [43] improve vehicle damage detection scenarios using Mask R-CNN.

After a thorough review of current literature, defect detection methods from point clouds can provide accurate results based on surface segmentation techniques. However, these methods have limitations in classifying different classes of damages. Moreover, surface segmentation is challenging to perform real-time defect detection due to the computational expense. In terms of image-based damage detection methods, the problem of damage detection on point cloud data can be addressed by CNN architectures. However, existing approaches focus on object detection or semantic segmentation of two-dimensional senses. Therefore, an accurate and automated damage area inspection and localization in 3D space is urgent for repair processes in the remanufacturing industry.

3. Proposed Damage Localization Framework

3.1 Framework Overview

This paper proposes an automated localization strategy based on deep learning and computer vision techniques for autonomous laser cladding repair processes. It focuses on improving the time efficiency of the identification and quantification of damage in piece parts, using cylindrical fixed bends as a case study. The localization is performed in two sequential steps: (1) a camera is used to identify the area in which the damage is located within the component, and (2) a laser triangulation sensor acquires an accurate volumetric representation of the damage for the laser cladding process to repair. Figure 2 shows a flowchart outlining the proposed damage localization pipeline in detail. The rationale behind the term 'hybrid localization framework' is the novel concurrent usage of a camera and a laser triangulation sensor that guide the repair process. Compared to current repair practices, the proposed method scans only the damaged surface autonomously instead of using manual inspection and scanning a larger area of the component, making it faster and consequently more cost-efficient while maintaining the accuracy and precision of the current repair process.
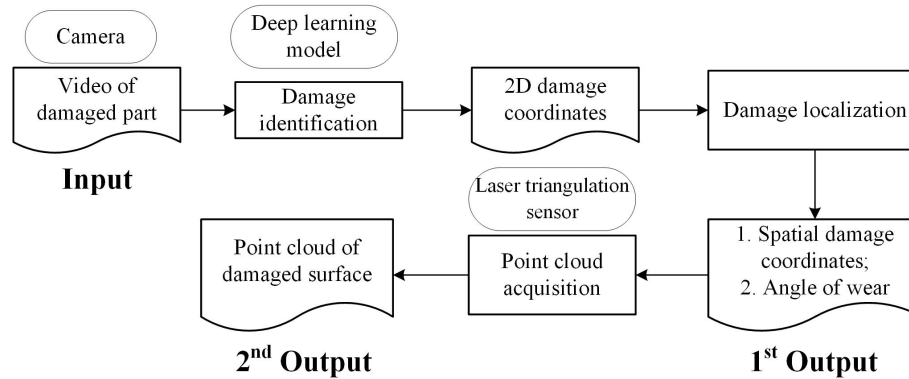
Figure 2. Hybrid damage localization framework.

The input to the framework is a video of the damaged component recorded by a camera. The stream of images is then run through a pre-trained deep learning model to automatically predict the location of the damage. The output from this deep learning model is a series or sequence of bounding boxes coordinates that represent the region of interest containing the damage. Using computer vision techniques, a damage localization process is carried out that uses those coordinates to obtain the location of the damage area in a 3-dimensional global reference frame.

A schematic of the proposed system for autonomous laser cladding repair processes is shown in Figure 3. The laser cladding head is attached to the robotic arm as an end-effector and installed laterally to the side of the laser head cover are the laser triangulation sensor and the camera. As an installation guideline, the sensors need to be as close as possible to the laser head and facing down towards the part to be repaired. Also, it is important that the sensors and the laser head are installed in parallel. This last requirement greatly simplifies the pre-processing and measurements required to deal with image transformations, so it is recommended, but other camera configurations can be used following the generic instructions mentioned below. This study focuses on damage identification and localization on cylindrical fixed bends, more specifically, the damage and the pad on fixed bends. These are mechanical parts used in the oil and gas industry. For worn fixed bends, it is essential to distinguish the location of the pad, as it is the area that incurs the most damage and must be repaired.
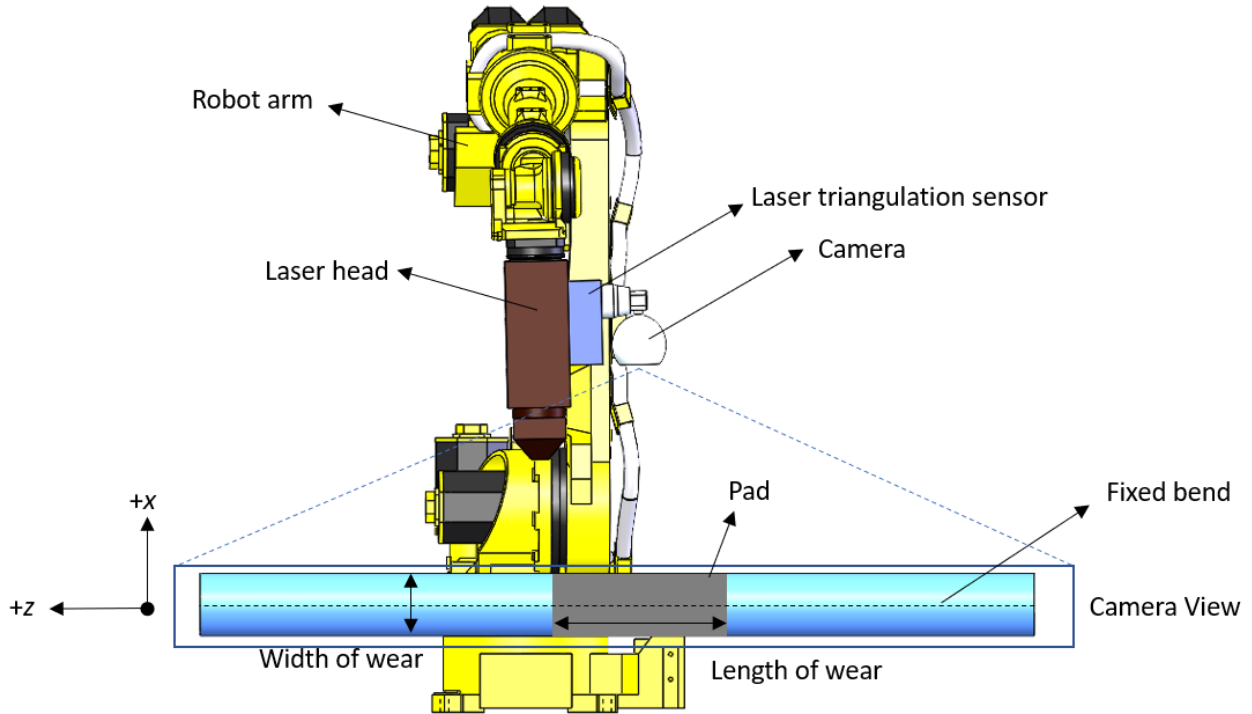
Figure 3. Model schematic of the proposed autonomous laser cladding repair system.

The following subsections describe the methods for damage identification and localization. Details of data acquisition and toolpath generation can be found in our previous research [9].

3.2 Damage Identification

The damage identification part of this framework follows the current research trends of using novel computational technologies to detect objects in images. Typical types of damage can be classified into wear, erosion, crack damage [44]. Point cloud acquisition technology by 3D scanning is challenging to characterize the erosion and crack damage ,therefore this study will focus on the wear damage. Some examples of wear damage on the fixed bends are as shown in Figure 4. Based on Imam et al. [9] recommendations for the identification of damage with regular or irregular shape in images of fixed bends, the use of deep learning models, namely Faster R-CNN, provides an accurate real-time detection tool to the system. That study tested several models and architectures around damage identification on similar fixed-bends and provided comparative results around the performance of deep learning models. Thus, this study builds upon the existing literature knowledge of applying convolutional neural networks (CNNs) for damage detection.
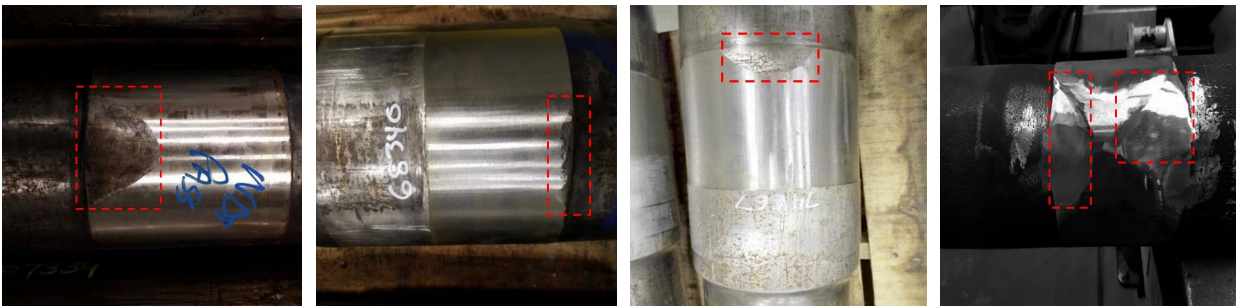

Figure 4. Examples of wear damages on fix bends (annotated by red dashed rectangles).

Faster R-CNN is an object detection architecture that consists of a feature extraction network, a region proposal network (RPN), and a region of interest (ROI) network. The function of a Faster R-CNN model is fourfold: 1) the pre-processed images go through a pre-trained CNN (e.g., ResNet or Inception) to extract features and acquire a feature map; 2) the RPN generates possible regions of interest in the feature map; 3) the ROI pooling extracts a feature vector of a fixed size from the feature map, and 4) the fixed-size feature map then goes through fully connected layers that predict the class label (classification) and the bounding box (regression) for each ROI.

Thus, a dataset is created to train the neural network selected. As shown in the model, the camera is fixed at the 'localization home' position during the inspection and localization process. Using that camera, 1048 original images (resolution: 1920 x 1080 pixels) of eight different fixed bends types are captured to form a dataset based on real historical data of an industrial setup in Edmonton, Canada. For this study, different types of geometric (horizontal flip and vertical flip) and photometric (grayscale, hue and exposure) augmentation techniques were applied to render the training model more robust and resilient to lighting and camera setting changes. Moreover, the images were resized to 416 x 416 pixels to reduce the training time. The dataset is then randomly split into 70% (733 images), 20% (210 images), and 10% (105 images) for training, validation, and testing purposes, respectively. An example of unlabeled images of the dataset can be found in Figure 5.
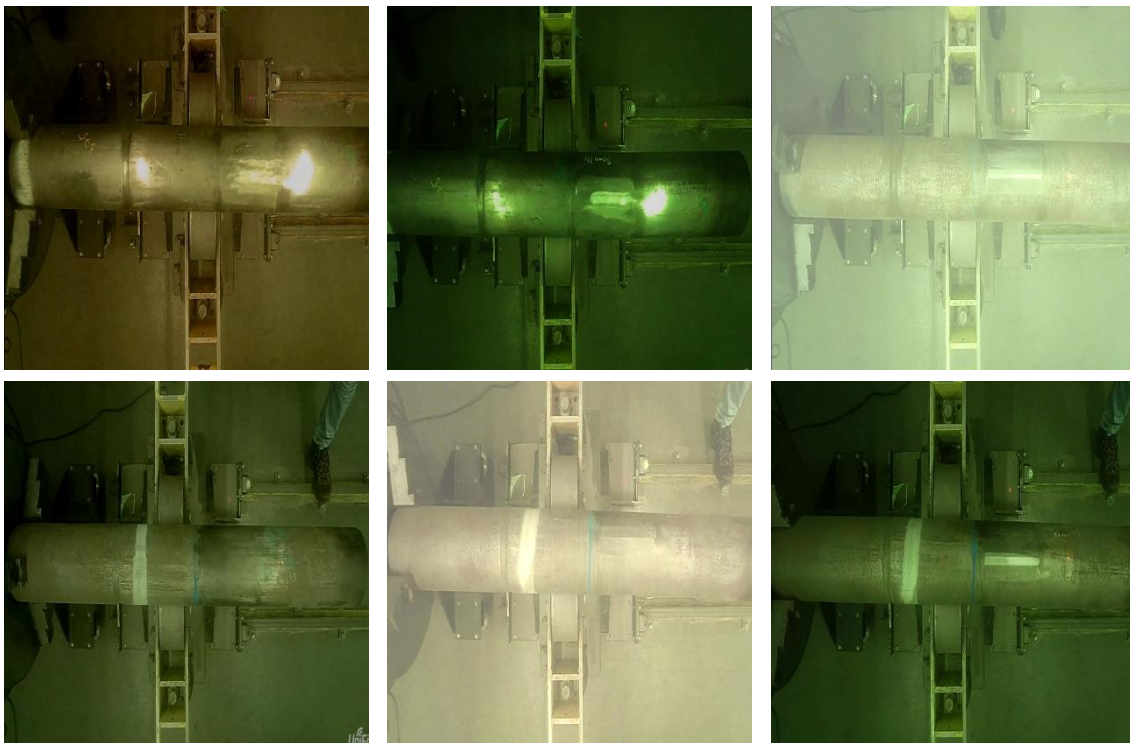

Figure 5. Sample images from the dataset.

The open-source TensorFlow object detection library version 1.5 is used in this study. Training scripts are carried out on Google Colaboratory (RAM ~ 12.6 GB, GPU: Tesla K80, 12 GB, Disk ~ 33GB). Applying the concept of transfer learning to ease computational efforts, the network is initialized with weights that are pretrained on the common objects in context (COCO) dataset. The feature extractors compared in this study are ResNet50 and Inception V2, again following Imam et al. results [9]. The training hyperparameters are summarized in Table 1, which are optimized to maximize prediction accuracy.

Table 1. List of optimized hyperparameters used during the training of the Faster R-CNN model.

Number of Steps	Batch Size	Learning Rate	Momentum Optimizer	Score Threshold
20000	12	0.001	0.9	0.2

This study primarily evaluates model performance based on their mean average precision (mAP) scores, as it is an extensively used metric for object detection [45]. Another factor to consider with real-time implementation is the time taken for inference per image. As such, both trained models are assessed on their mAP scores and their detection speed, and the results are listed in Table 2. The publicly available mAP values resulting from the COCO dataset are also listed for reference. The resulting metric plots obtained from the best-performing model (ResNet 50) are illustrated in Figure 6.

Table 2. Comparative performance analysis of the architectures on the training and validation datasets.

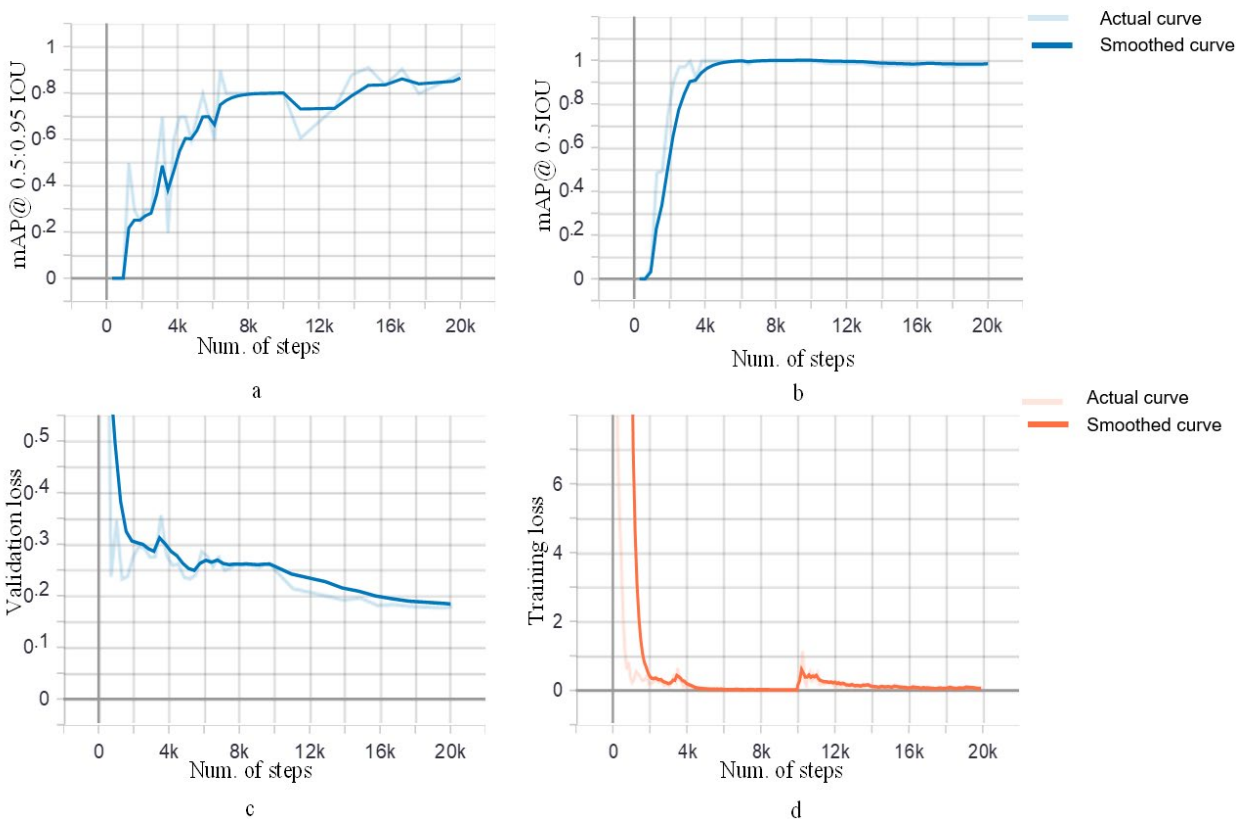| Architecture	'Fixed Bends' mAP	COCO mAP	Detection speed (ms/image)
ResNet50	**88.7%**	30%	1.48
Inception v2	79.4%	28%	**1**

Figure 6. Training results of the R-CNN models using the fixed bends dataset. (a) mAP @ 0.5:0.95 IOU & (b) mAP @ 0.5 IOU; (c) validation loss and (d) training loss.

The application of the Faster R-CNN model provides then a classification result that confirms that the damage found is of interest for the repair process and a bounding box that support the localization of the damage in the camera image. This bounding box is defined, for each detection, by four points $(p_1, \ldots, p_4)$. From those points, the length (l_{BB}) and width (w_{BB}) of the bounding box can be calculated.

3.3 Damage Localization

3.3.1 Camera Calibration

Calibration is an essential prerequisite for the utilization of a camera in an autonomous repair system as it determines the accuracy of any image-based measurement. An imprecise calibration influences all parts of an autonomous repair framework, leading to inaccurate localization, scanning, and laser cladding results. Knowledge of both intrinsic and extrinsic parameters of the camera is required for a true projection of a 3-dimensional point in space to a 2-dimensional image point. Herein, the intrinsic parameters represent the internal characteristics of the camera, e.g., the optical center and the focal length, whereas the extrinsic parameters determine the orientation of the camera in the real-world space. Using the pinhole camera model, the relationship between the global coordinates and the camera coordinates is shown below:

$$\begin{bmatrix} u \\ v \\ 1 \end{bmatrix} = A[\boldsymbol{R} \quad \boldsymbol{T}] \begin{bmatrix} X \\ Y \\ Z \\ 1 \end{bmatrix}; \; with \; A = \begin{bmatrix} \alpha & 0 & u_0 \\ 0 & \beta & v_0 \\ 0 & 0 & 1 \end{bmatrix}, \boldsymbol{R} = \boldsymbol{R}_z \, \boldsymbol{R}_y \, \boldsymbol{R}_x \, , and \; \boldsymbol{T} = \begin{bmatrix} t_x \\ t_y \\ t_z \end{bmatrix} \tag{1}$$

$$\boldsymbol{R}_x = \begin{bmatrix} 1 & 0 & 0 \\ 0 & \cos\theta_x & -\sin\theta_x \\ 0 & \sin\theta_x & \cos\theta_x \end{bmatrix}; \; \boldsymbol{R}_y = \begin{bmatrix} \cos\theta_y & 0 & \sin\theta_y \\ 0 & 1 & 0 \\ -\sin\theta_y & 0 & \cos\theta_y \end{bmatrix}; \boldsymbol{R}_z = \begin{bmatrix} \cos\theta_z & -\sin\theta_z & 0 \\ \sin\theta_z & \cos\theta_z & 0 \\ 0 & 0 & 1 \end{bmatrix} \tag{2}$$

where (u, v) are the 2-dimensional horizontal and vertical image coordinates respectively and (X, Y, Z) are the 3-dimensional coordinates in the global reference frame; (A) is the camera intrinsic matrix with (α) and (β) being the focal lengths expressed in pixel units, (u_0, v_0) are the image coordinates of the principal point, which is usually at the image center; and $[\boldsymbol{R} \quad \boldsymbol{T}]$ represents an extended matrix containing the rotational and translational matrices required to transform the camera reference frame to the global reference frame, called the extrinsic matrix of the model. The intrinsic matrix is obtained using well-known open-source camera calibration methods [46], and the extrinsic matrix is estimated by measuring the distances in the proper axes between the camera and the global reference frame. Finally, the 3-dimensional global coordinates of the damaged area can be calculated as:

$$\begin{bmatrix} X \\ Y \\ Z \\ 1 \end{bmatrix} = [\boldsymbol{R} \quad \boldsymbol{T}]^{-1} A^{-1} \begin{bmatrix} u \\ v \\ 1 \end{bmatrix} \tag{3}$$

which can be simplified to the following equation to calculate X, Y and Z:

$$\begin{bmatrix} X \\ Y \\ Z \end{bmatrix} = \left(\begin{bmatrix} u \\ v \\ 1 \end{bmatrix} A^{-1} - \boldsymbol{T} \right) \boldsymbol{R}^{-1} \tag{4}$$

In this study, the camera calibration is key to transforming the bounding box points detected in the image to real 3-dimensional points in the fixed bend that the system can use to guide the repair process. The transformation of each point of the bounding box, $p = (u_{BB}, v_{BB})$, into a point in the real world, $(P = (X_{BB}, Y_{BB}, Z_{BB})$, follows Equation 4.

3.3.2   *Localization in Rotating Cylindrical Parts*

To finalize the localization of the damage on the fixed bend, the system quantifies how much the area where the damage is certainly located encircles the cylindrical surface. For this, the fixed bend is rotated while the camera stores away the video feed. This is required due to two reasons: (1) doing a full rotation of the fixed bend, it is ensured that the damage is exposed to the camera; and (2) usually damage spans along the surface of the fixed bend further than the field of view of the camera, so using a single shot to locate all the damage is not possible.

The video is recorded at a known frame rate (f) while rotating the turntable counterclockwise at a set angular speed, (ω). The camera used in this study has a motion-capture sensor, so it automatically records any motion in the field of view, triggering the video recording sequence as the part rotates. If that were not the case, other options to add the camera recording sequence to the power-on of the part rotation should be explored. The part rotation is recorded by the camera, such that the first frame corresponds to a 0 degrees rotation and the last frame corresponds to a full 360 degrees rotation.

Therefore, using the trained Faster R-CNN model, a series of bounding boxes are obtained overtime at the camera framerate. An example for the testing dataset with bounding box output is shown in Figure 7, and P_1 to P_4 are the corners for the bounding box. From those detections, the damage size can be quantified for each frame following Equation 5.

$$\forall \text{frame}, \begin{cases} l_{\text{BB}} = \|P_1 - P_2\| = \|P_3 - P_4\| \\ w_{\text{BB}} = \|P_1 - P_3\| = \|P_2 - P_4\| \end{cases} \tag{5}$$
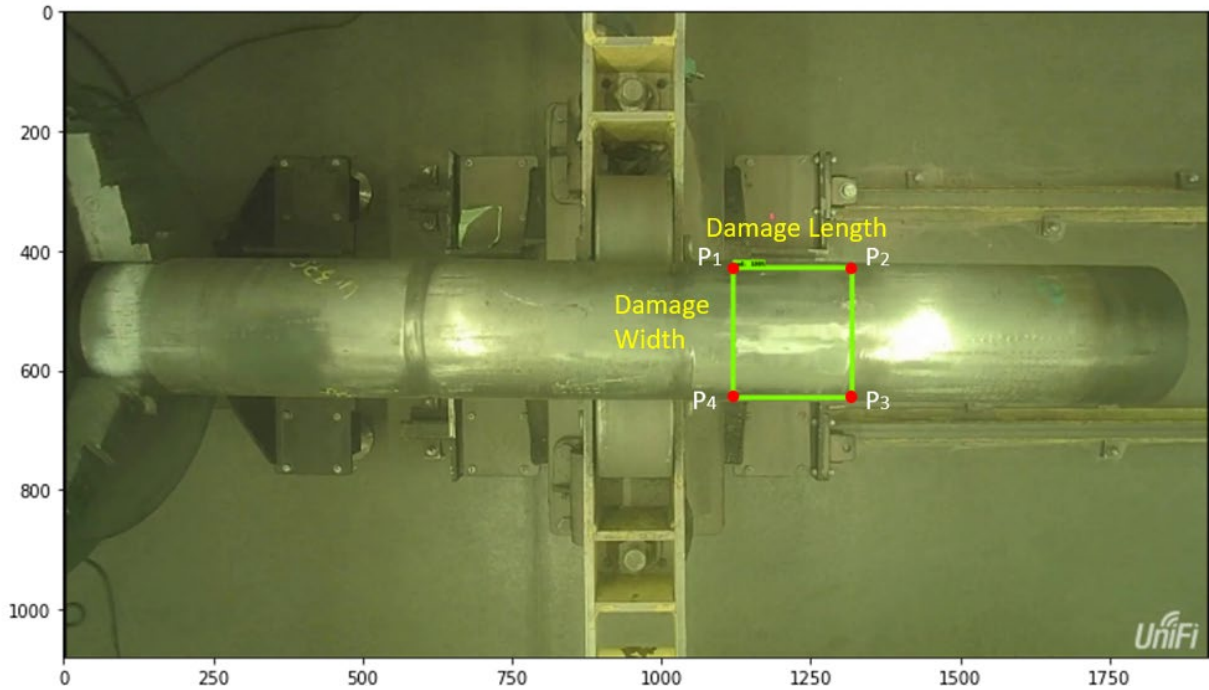

Figure 7. A figure from the testing dataset with bounding box output.

Therefore, for the whole video sequence, a range of damage lengths (l_{BB}) and widths (w_{BB}) is obtained. An example of the video sequence results for both parameters is illustrated in Figure 8 (false and missed detections are omitted in the figure). As expected, during the video sequence, each frame outputs one damage length and width. As the model starts to detect the damage on the part, the length measurement is quite a constant bar certain variance of the model, but the width measurement increases and decreases as the damage appears on the camera field of view. Thus, the measurements obtained cannot be taken from the bounding box results at face value.
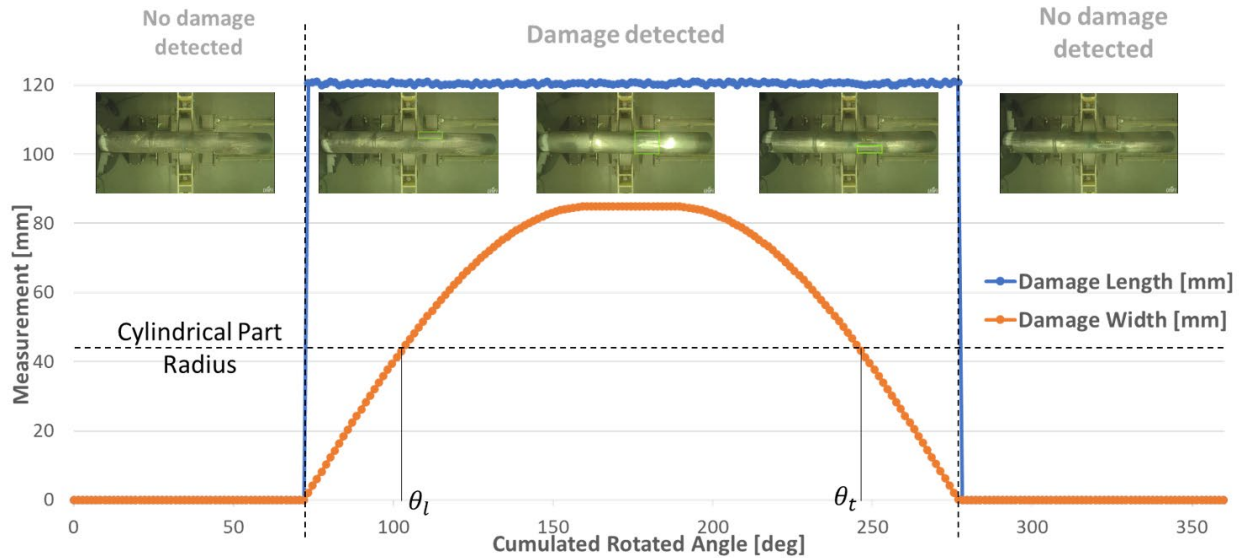

Figure 8. Measured length and width of the damaged pad in a fixed bend part over a full rotation.

Let a damage of a cylindrical component be defined by its length and its angle, as shown in Figure 9. The length of the damage (L_{BB}), may be obtained as an estimation of the bounding box length results; however, the angle of damage (θ_D), which starts at the leading angle (θ_l) and ends at the trailing angle (θ_t) requires additional effort.
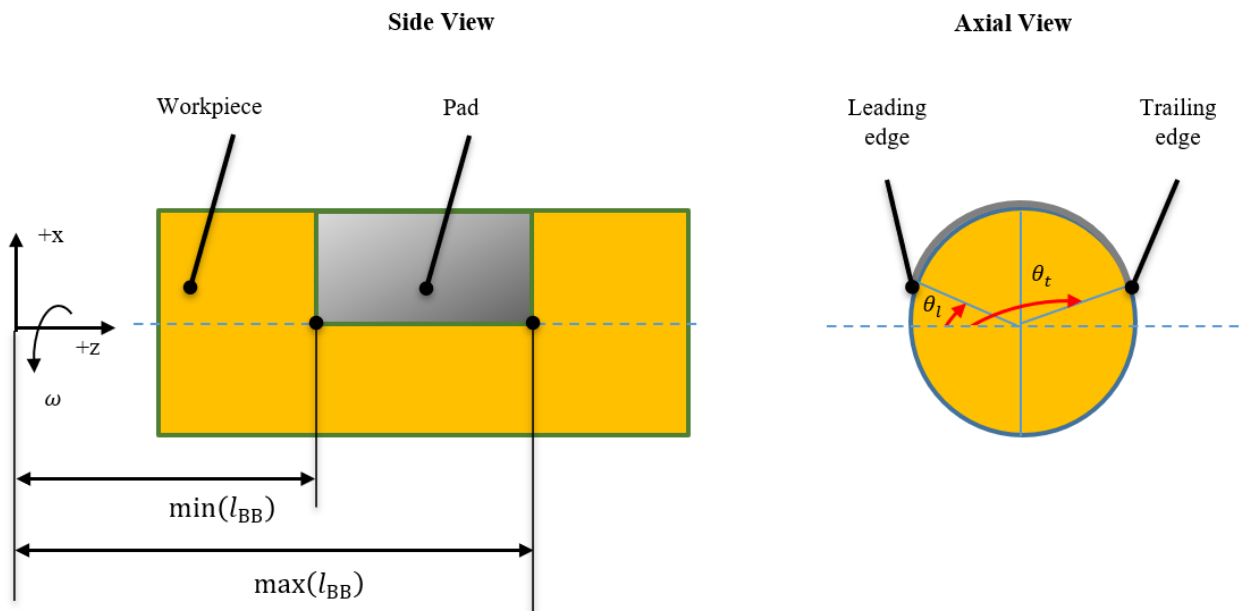

11

Figure 9. Side view and axial view demonstrating the length and angle of the damage over a cylindrical component.

The angle of damage goes chronologically from (θ_l) to (θ_t). As the part rotates, the leading edge of the damage always appears in the image first, followed by the trailing edge. Considering that all repair operations occur over the symmetry axis of the cylindrical part, the leading and trailing angles need to use the reference frame for their localization. As such, the angles are obtained when the width of the bounding box accounts for the radius of the cylindrical part, satisfying Equation 6.

$$N_i = \{n, m \mid w_{\mathrm{BB}_i} = r\} \tag{6}$$

where (n) and (m) are the elapsed number of frames in the video sequence when the width of the bounding box is exactly the cylindrical part radius (r). With that, the angles can be calculated using Equation 7 below.

$$\forall N, \begin{cases} \theta_l = n\,{}^{\omega}\!/_{f} \\ \theta_t = m\,{}^{\omega}\!/_{f} \end{cases} \tag{7}$$

where (θ_l) and (θ_t) stand for the angular coordinates of the leading edge and trailing edge, respectively, and (ω) and (f) represent the angular velocity of the rotary table and the camera framerate, respectively. Finally, the length of the damage (L_D), and angle of damage (θ_D), serve as input to the laser triangulation sensor to scan the damaged surface of the cylinder. They determine the area's boundaries to scan that will guide the robotic arm and rotary table during the scanning process. Both parameters are calculated following Equation 8.

$$\begin{cases} \theta_D = \theta_t - \theta_l \\ L_D = \max(l_{\mathrm{BB}}) - \min(l_{\mathrm{BB}}), \text{if } l_{\mathrm{BB}} \neq 0 \end{cases} \tag{8}$$

4. Results

4.1 Autonomous Robotic Laser Cladding Repair Cell

A UVC-G3-Bullet/UVC-G3-AF camera and a Keyence IL-300 laser triangulation sensor are fitted on the laser head in a way that both the sensors are parallel to the laser head and are facing down at a right angle to the part axis. The camera operates at 30 frames per second. As stated before, this arrangement eliminates tedious angle measurements, simplifying the camera's mathematical model, which is the author's recommendation as to the easiest hardware setting. The origin of the global coordinate system is in the center of the turntable, as annotated in Figure 10. The damaged cylindrical component will be mounted on this turntable for damage localization and repair.
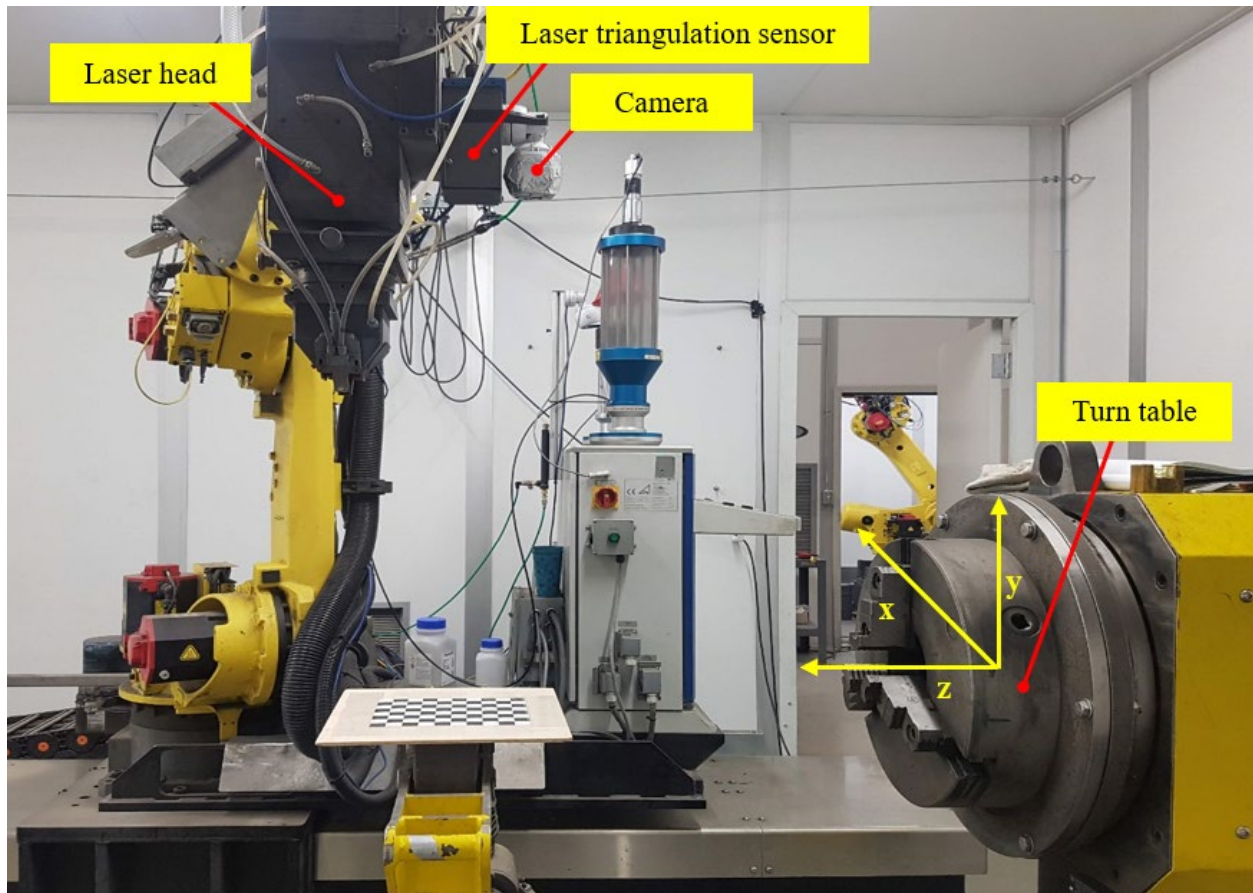
Figure 10. Image of the experimental setup during the calibration process with its main components highlighted.

To ensure consistency, the Fanuc-R-1000iA/80F robot arm moves to a fixed position called 'localization home' before spatially localizing each damaged component. At the 'localization home' position, the laser head's pose with respect to the turntable is set and is saved in the system's memory. It is important to note here that the coordinates of the laser head with respect to the global world frame can be read off from the machine at this position. However, for camera calibration, the position of the camera lens with respect to the global origin must be known. A schematic showing the entire setup with the arrangement of the camera from a side view and an axial view is shown in Figure 11 (all units in that figure are in millimeters). The offset between the camera lens and the turntable is measured manually from the experimental setup. The side view shows the offset of the camera lens to the turntable in the z-direction, i.e., 499 mm, whereas the axial view indicates the offset in the x and y direction, which is -10 mm and 700 mm, respectively.
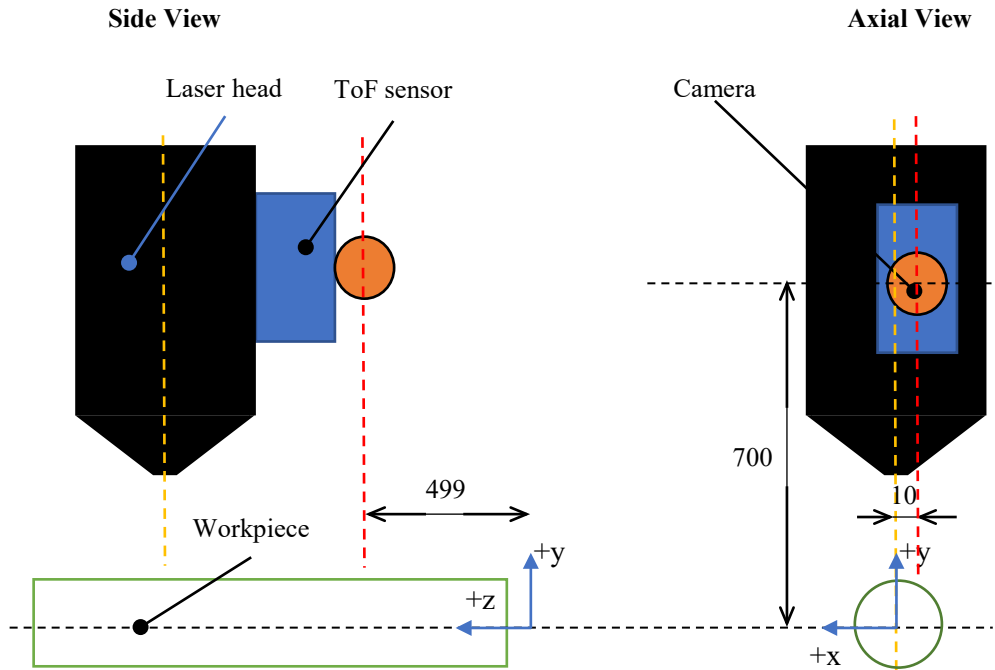
Figure 11. Camera offsets (in mm) schematics from the global coordinate origin.

The damaged component is mounted on the turntable that rotates it along the cylinder's longitudinal axis, which is aligned with the center of the turntable. This rotational motion is defined by the angular velocity of the turntable (ω), which is fixed to 41.54 degrees per second or 0.725 radians per second. To ensure there is no bending of the part due to only one of its ends being fixed, the straightness of its axis is scrutinized with a spirit level. The camera has a motion sensor that automatically records a video once it detects movement. Exploiting this feature, the turntable is rotated at a known angular velocity, and the video is recorded for one complete rotation. Figure 12 shows the perspective of the damaged part from the camera. Here, the camera has a top view of the part such that the length of wear is on the z axis and the width of wear is on the x axis.
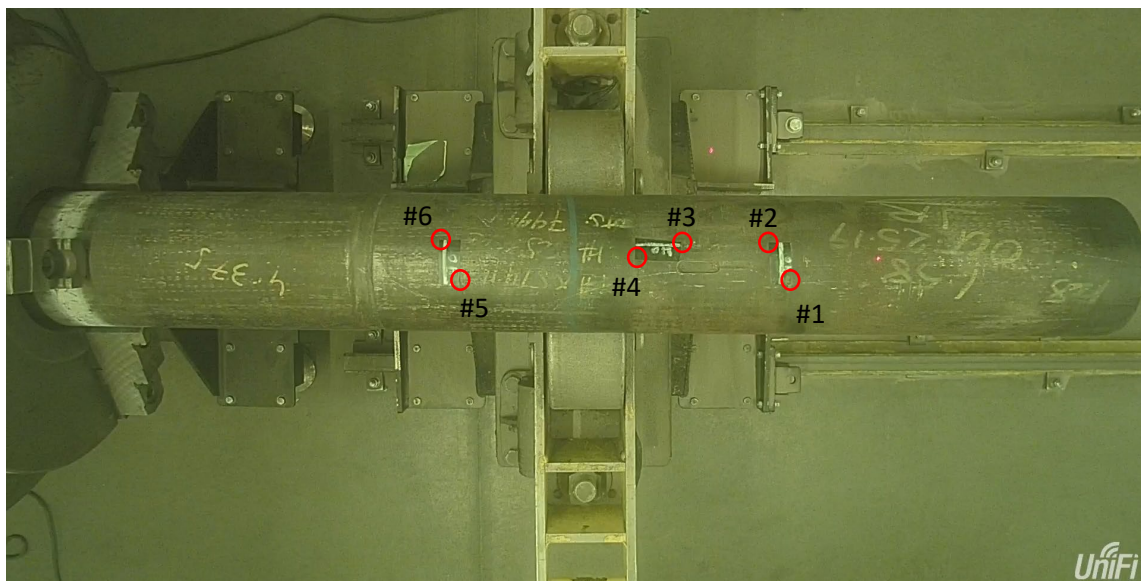
Figure 12. Camera top view of the experimental case study with the tape markers with known edge coordinates for calibration validation.

To ensure the robotic repair cell is adequately calibrated and quantifies calibration errors, a validation process is performed. The calibration intrinsic and extrinsic matrices are outlined in Table 3, along with the physical inherent projection error of the camera. A fixed bend is mounted on the turntable, and three equal lengths of black tape are applied to its surface. The edges of the tapes are annotated with circles in red (see Figure 12). The robot is moved to its 'localization home' position and an image is captured. The real-world coordinates representing the edges of the three tapes are then measured and recorded. Based on the pixel coordinates obtained from the image, the world coordinates of each point are calculated.

Table 3. Algorithm for the intersection part modification problem.

Mean projection error [mm]	Intrinsic matrix	Extrinsic matrix
0.17	$A = \begin{bmatrix} 1284 & 0 & 950 \\ 0 & 1280 & 562 \\ 0 & 0 & 1 \end{bmatrix}$	$[\mathbf{R} \quad \mathbf{T}] = \begin{bmatrix} 0 & 0 & 1 & -10 \\ -1 & 0 & 0 & 700 \\ 0 & -1 & 0 & 499 \end{bmatrix}$

The performance of the proposed calibration model is assessed by calculating the root mean square error, which follows Equation 9 below:

$$\Delta = \sqrt{(x_i - x)^2 + (y_i - y)^2 + (z_i - z)^2} \tag{9}$$

where $(x_i), (y_i), (z_i)$ are the estimated world coordinates of the pad locations based on the camera model; and $(x), (y),$ and (z) are the real-world coordinates taken manually by guiding the robot arm to the pad location. The relative error percentage is then defined by Equation 10 and the calibration results for all the points used in the calibration setup are listed in Table 4.

$$r = \frac{\Delta}{\sqrt{x^2 + y^2 + z^2}} \tag{10}$$

Table 4. Validation of the calibration setup using tape markers.

	x	y	z	x_i	y_i	z_i	Δ (mm)	r	e_z (mm)
#1	-16.3	56.8	674.3	-13.969	59.812	682.972	9.471	1.40%	8.672
#2	18.4	57.4	656.7	21.512	62.41	664.981	10.167	1.54%	8.281
#3	19.1	57.2	583	21.901	61.115	591.211	9.518	1.62%	8.211
#4	4.3	57.6	544.2	7.888	60.091	552.495	9.375	1.71%	8.295
#5	-17.7	56.9	395.5	-15.46	59.327	406.29	11.284	2.82%	10.79
#6	20.3	56.8	376.7	23.589	59.165	389.343	13.276	3.48%	12.643
Mean							10.515	2.10%	9.482
Standard Deviation							1.531	0.85%	1.834

From these error values, an error margin can be calculated that needs to be added to the calculated axial (z) coordinate to ensure the pad is entirely represented by the coordinates and account for hardware measurement errors. This is illustrated in Figure 13, where $(\bar{e}_z)$ and (s_z) are the mean and the standard deviation of the error in the z-axis, respectively. Assuming the error values in z follow a normal distribution, an interval of 95% confidence is obtained adding and subtracting two times (s_z) and $(\bar{e}_z)$ to the coordinates of (L_D), the damage length.
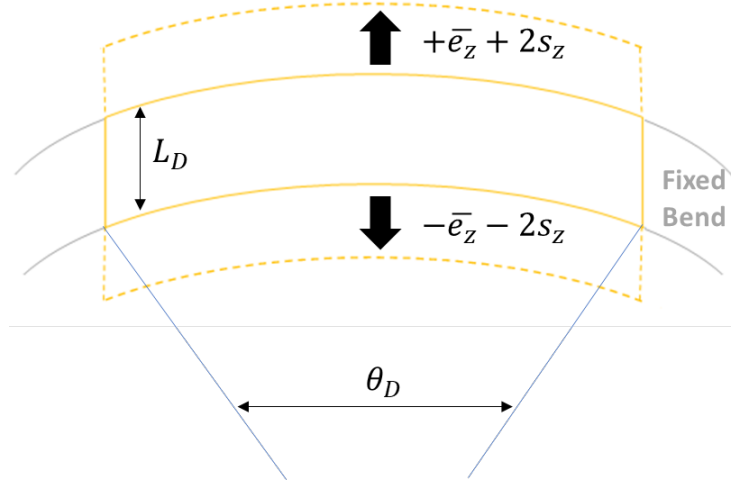
Figure 13. Schematic of the error tolerance introduced along the *z* axis to account for the calibration error.

4.2 Validation Results

This section presents two case studies that aim to validate the damage localization framework for autonomous robotic laser cladding repair processes. These case studies are carried out on two different parts with varying radii. Following are the results from the case studies and how they compare to the measured or actual value. It is important to note that the length of the damage is manually measured with a measuring tape (accuracy: 1 millimeter), and the angle was noted by reading the angular coordinate of the turntable at the location of the leading edge and the trailing edge (accuracy: 1 degree).

1.1.1 Case Study 1

The first case study is done over a fixed bend of 60 millimeters of the radius with a known pad length and damage angle, as shown in Figure 14a. From the inference, 262 frames are recorded while the fixed bend rotates. Using the proposed framework, the results for this case study are tabulated in Table 5. The results show a total angular displacement error of 0.408° and a length error of 9.91 mm. Considering the accuracy of the measurement devices, the angular error is considered negligible, and the length error is inferior to the tolerancing applied. Therefore, the coordinates containing the repair patch with the error tolerance added are sent to the laser triangulation sensor, and the equivalent point cloud is obtained, as shown in Figure 14b. The time it takes to acquire the point cloud of the damaged surface is 16 minutes, whereas obtaining the entire surface geometry would take 45 minutes.

Table 5. List of results from case study 1.

	θ_D	L_D (mm)
Measured	120°	120
Calculated	120.408°	129.91
Error	0.408° (0.34%)	9.91 (8.26%)

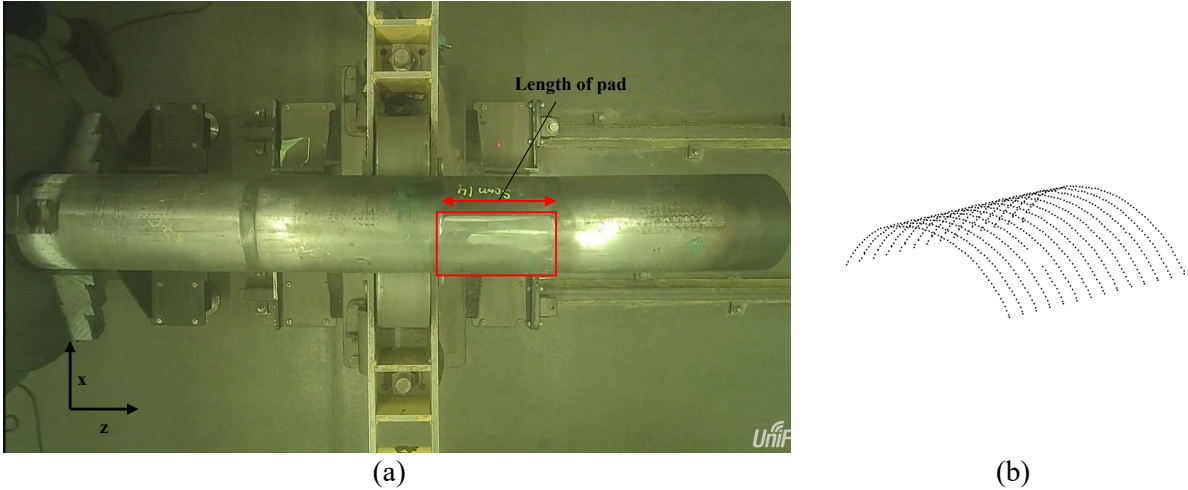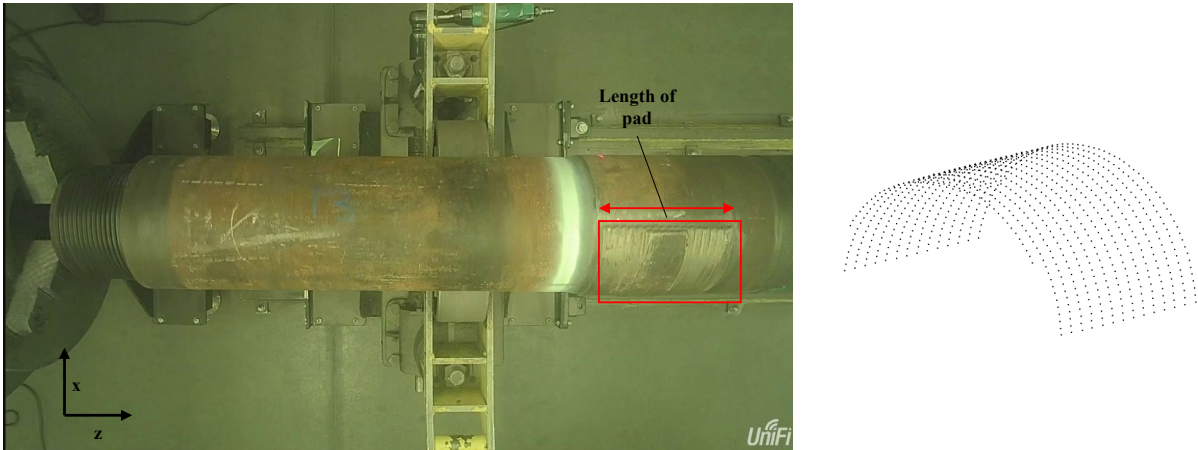|	(a)		(b)

Figure 14. Illustration of the results for case study 1. (a) Sample image from the camera with the pad and axes annotated; (b) Scanned point cloud representing the damage in the fixed bend.

1.1.2 Case Study 2

The second case study is done over a fixed bend of 91 millimeters of the radius with a known pad length and damage angle, as shown in Figure 15a. From the inference, 275 frames are recorded while the fixed bend rotates. Using the proposed framework, the results for this case study are tabulated in Table 6. The results show a total angular displacement error of 0.72° and a length error of 0.17 mm. Similarly, these errors are within the expected results, and the coordinates containing the repair patch with the error tolerance added are sent to the laser triangulation sensor. The point cloud is obtained, as shown in Figure 15b.

Table 6. List of results from case study 2.

	θ_D	L_D (mm)
Measured	110°	150
Calculated	110.72°	149.83
Error	0.72° (0.65%)	0.17 (0.11%)

17

Figure 15. Illustration of the results for case study 2. (a) Sample image from the camera with the pad and axes annotated; (b) Scanned point cloud representing the damage in the fixed bend.

4.3 Discussion

In summary, the proposed visual system is capable of identifying the damaged area of the cylindrical component. Even though the neural network may fail to detect or incorrectly detects the pad, the damage localization relies on a sequence of images (or video), thus such outliers can be easily filtered out. Nonetheless, it is important to note that the final damage area estimated can be smaller than the real damage area, such as in case study 2, where the measured damaged damage is slightly larger than the estimated by the system. Indeed, the consideration of errors in the angle and length estimations are key to ensuring the correct registration of the entire damaged area. In this study, the errors are directly correlated to the algorithms and systems' precision and accuracy. However, to support the autonomous operation of the robotic repair cell, a minimum error margin might be advisable, independently of the detection accuracy, as a safeguard. This would minimize the risk of performing a partial repair on a damaged part. Also, a post-repair inspection process with the same system could be developed to ensure the quality of the laser cladding process and of the repaired unit.

Overall, the proposed system significantly reduces the time the point cloud acquisition process takes by introducing an additional process and visual system. With this approach, the time for the system to capture the video and finally acquire the point cloud for the first and second case studies are 16 and 20 minutes, respectively. If it were to capture the entire surface geometry (current industrial practice), it would take around 45 and 54 minutes for case studies 1 and 2, respectively. Therefore, a time reduction of 64.4% (29 minutes) and 63.0% (34 minutes) is achieved.

In fact, analyzing the process itself, this approach is interesting for all kinds of repair processes where the ratio of damage area per current registered area is small. In other words, if from the current scanning process the usable data is a small fraction of the total scanned data, then the proposed approach might be worth investigating to increase productivity by reducing waste, i.e., the time it takes to generate and process the point cloud outside the damaged area. Also, optimizing the use of the laser scanner diminishes the process cost as lesser maintenance costs are expected per repaired unit. Nonetheless, further analysis on the cost-effectiveness and impact of these changes on a fully autonomous laser cladding repair cell is in process.

5. Conclusions

Repair or remanufacturing is a green manufacturing strategy that helps to reduce industrial waste by reducing cost, energy, and, most importantly, material consumption. Damage localization is a crucial step in repair that typically relies heavily on a human operator. The proposed robotic laser cladding repair system is able to autonomously locate and quantify the damaged areas on worn components. In order for the laser triangulation sensor to autonomously scan only the damaged region, the robotic system needs to be calibrated so that two-dimensional information from a camera can be translated into three-dimensional global coordinates. To achieve this, the camera in the RLCRC is calibrated, and the calibration parameters with respect to the global coordinate origin are found. Since the damaged region wraps around a cylindrical part's surface, the main goal is to obtain the longitudinal and angular coordinates of the damaged patch.

The damaged part is mounted on the turntable, and the robot arm is moved to the 'localization home' position. The turntable is rotated for a full 360°, and whilst it rotates, a video is recorded for the deep learning model to identify and localize the damaged region on 2D image data. Based on the spatial localization parameters presented in section 2.3, this information is converted to 3D world coordinates providing the axial and angular ranges of the damaged region. To corroborate the 2D to 3D conversion, a validation between the measured and calculated 3D coordinates is conducted that shows an average relative

error of 2.018%. Moreover, two case studies are presented where the calculated length and angle of wear are compared to the measured values. For case study 1, the results show a length error of 9.91mm and an angular displacement error of 0.408°, respectively. For case study 2, the length and angular displacement errors are 0.17 mm and 0.72°, respectively. In summary, the proposed approach reduces the time for localization and registration of damaged parts for repair by almost 63% and consequently increases productivity and decreases the cost of the laser cladding repair process. This study supports the viability of an autonomous laser cladding repair process for cylindrical components by the use of vision systems to automatically localize and optimize the registering process.

So far, the method has only been proved effective in repairing the cylindrical part. For the general situation, other types of parts, especially parts with free-form surfaces should be explored in future work. Moreover, detection and localization of damages at different regions of the worn part should also be focused on in the future. Finally, other point cloud acquisition devices (e.g. profilometer, high-precise 3D camera) can be investigated to improve the time reduction in the scanning process.

2   Acknowledgments

3   References

[1]   Lee CM, Woo WS, Roh YH. Remanufacturing: Trends and issues. Int J Precis Eng Manuf - Green Technol 2017;4:113–25. https://doi.org/10.1007/s40684-017-0015-0.

[2]   Zheng Y, Mamledesai H, Imam H, Ahmad R. A novel deep learning-based automatic damage detection and localization method for remanufacturing/repair. Comput Aided Des Appl 2021;18:1359–72. https://doi.org/10.14733/cadaps.2021.1359-1372.

[3]   Jiang Z, Zhou T, Zhang H, Wang Y, Cao H, Tian G. Reliability and cost optimization for remanufacturing process planning. J Clean Prod 2016;135:1602–10. https://doi.org/10.1016/j.jclepro.2015.11.037.

[4]   Zheng Y, Ahmad R. Feature extraction and process planning of integrated hybrid additive-subtractive system for remanufacturing. Math Biosci Eng 2020;17:7274–301. https://doi.org/10.3934/MBE.2020373.

[5]   Zheng Y, Liu J, Ahmad R. A cost-driven process planning method for hybrid additive–subtractive remanufacturing. J Manuf Syst 2020;55:248–63. https://doi.org/10.1016/j.jmsy.2020.03.006.

[6]   Liu J, Zheng Y, Ma Y, Qureshi A, Ahmad R. A Topology Optimization Method for Hybrid Subtractive–Additive Remanufacturing. Int J Precis Eng Manuf Technol 2019. https://doi.org/10.1007/s40684-019-00075-8.

[7]   Raj D, Maity SR, Das B. State-of-the-art review on laser cladding process as an in-situ repair technique. Proc Inst Mech Eng Part E J Process Mech Eng 2021. https://doi.org/10.1177/09544089211044558.

[8]   Gharbi M, Peyre P, Gorny C, Carin M, Morville S, Le Masson P, et al. Influence of a pulsed laser regime on surface finish induced by the direct metal deposition process on a Ti64 alloy. J Mater

Process Technol 2014;214:485–95. https://doi.org/10.1016/j.jmatprotec.2013.10.004.

[9] Imam HZ, Zheng Y, Martinez P, Ahmad R. Vision-Based Damage Localization Method for an Autonomous Robotic Laser Cladding Process. Procedia CIRP 2021;104:827–32. https://doi.org/10.1016/j.procir.2021.11.139.

[10] Westkämper E. Strategic Development of Factories under the Influence of Emergent Technologies. CIRP Ann - Manuf Technol 2007;56:419–22. https://doi.org/10.1016/j.cirp.2007.05.100.

[11] Zhang X, Li W, Chen X, Cui W, Liou F. Evaluation of component repair using direct metal deposition from scanned data. Int J Adv Manuf Technol 2017:1–14. https://doi.org/10.1007/s00170-017-1455-y.

[12] Zhang X, Li W, Liou F. Damage detection and reconstruction algorithm in repairing compressor blade by direct metal deposition. Int J Adv Manuf Technol 2017. https://doi.org/10.1007/s00170-017-1413-8.

[13] Ma J, Zhao J, Yuille AL. Non-rigid point set registration by preserving global and local structures. IEEE Trans Image Process 2016;25:53–64. https://doi.org/10.1109/TIP.2015.2467217.

[14] Zhang X, Cui W, Liou F. Voxel-Based Geometry Reconstruction for Repairing and Remanufacturing of Metallic Components Via Additive Manufacturing. Int J Precis Eng Manuf - Green Technol 2021:291–7. https://doi.org/10.1007/s40684-020-00291-7.

[15] Pomerleau F, Colas F, Siegwart R. A Review of Point Cloud Registration Algorithms for Mobile Robotics. Found Trends Robot 2015;4:1–104. https://doi.org/10.1561/2300000035.

[16] Aprilia A, Nguyen WLK, Khairyanto A, Pang WC, Tor SB, Seet G. Towards automated remanufacturing process with additive manufacturing. Proc Int Conf Prog Addit Manuf 2018;2018-May:696–701. https://doi.org/10.25341/D4SW2N.

[17] Li L, Li C, Tang Y, Du Y. An integrated approach of reverse engineering aided remanufacturing process for worn components. Robot Comput Integr Manuf 2017;48:39–50. https://doi.org/10.1016/j.rcim.2017.02.004.

[18] Geng Z, Bidanda B. Review of reverse engineering systems–current state of the art. Virtual Phys Prototyp 2017;12:161–72. https://doi.org/10.1080/17452759.2017.1302787.

[19] Nguyen A, Le B. 3D point cloud segmentation: A survey. IEEE Conf Robot Autom Mechatronics, RAM - Proc 2013:225–30. https://doi.org/10.1109/RAM.2013.6758588.

[20] Jiang XY, Meier U, Bunke H. Fast range image segmentation using high-level segmentation primitives. IEEE Work Appl Comput Vis - Proc 1996:83–8. https://doi.org/10.1109/acv.1996.572006.

[21] Sappa AD, Devy M. Fast range image segmentation by an edge detection strategy. Proc Int Conf 3-D Digit Imaging Model 3DIM 2001;2001-Janua:292–9. https://doi.org/10.1109/IM.2001.924460.

[22] Pu S, Vosselman G. Automatic extraction of building features from terrestrial laser scanning. Int Arch Photogramm 2006;36:25–7. https://doi.org/10.1.1.222.2486.

[23] Rusu RB, Marton ZC, Blodow N, Dolha M, Beetz M. Towards 3D Point cloud based object maps for household environments. Rob Auton Syst 2008;56:927–41. https://doi.org/10.1016/j.robot.2008.08.005.

[24] Köster K, Spann M. MIR: An approach to robust clustering - application to range image segmentation. IEEE Trans Pattern Anal Mach Intell 2000;22:430–44. https://doi.org/10.1109/34.857001.

[25] Biosca JM, Lerma JL. Unsupervised robust planar segmentation of terrestrial laser scanner point clouds based on fuzzy clustering methods. ISPRS J Photogramm Remote Sens 2008;63:84–98. https://doi.org/10.1016/j.isprsjprs.2007.07.010.

[26] Filin S. Surface clustering from airborne laser scanning data. Int Arch Photogramm Remote Sens Spat Inf Sci 2001;34:119–124.

[27] Vosselman G, Dijkman S. 3D building model reconstruction from point clouds and ground plans. Int Arch Photogramm Remote Sens 2001;XXXIV:37–43.

[28] Hitchcox T, Zhao YF. Random walks for unorganized point cloud segmentation with application to aerospace repair. Procedia Manuf 2018;26:1483–91. https://doi.org/10.1016/j.promfg.2018.07.093.

[29] Jovančević I, Pham HH, Orteu JJ, Gilblas R, Harvent J, Maurice X, et al. 3D Point Cloud Analysis for Detection and Characterization of Defects on Airplane Exterior Surface. J Nondestruct Eval 2017;36. https://doi.org/10.1007/s10921-017-0453-1.

[30] Zheng Y, Liu J, Liu Z, Wang T, Ahmad R. A primitive-based 3D reconstruction method for remanufacturing. Int J Adv Manuf Technol 2019:3667–81. https://doi.org/10.1007/s00170-019-03824-w.

[31] Zheng Y, Qureshi AJ, Ahmad R. Algorithm for remanufacturing of damaged parts with hybrid 3D printing and machining process. Manuf Lett 2018;15:38–41. https://doi.org/10.1016/j.mfglet.2018.02.010.

[32] Kashani AG, Graettinger AJ. Cluster-Based Roof Covering Damage Detection in Ground-Based Lidar Data. Autom Constr 2015;58:19–27. https://doi.org/10.1016/j.autcon.2015.07.007.

[33] Shinozaki Y, Kohira K, Masuda H. Detection of deterioration of furnace walls using large-scale point-clouds. Comput Aided Des Appl 2018;15:575–84. https://doi.org/10.1080/16864360.2017.1419645.

[34] Zeng J, Chang B, Du D, Hong Y, Zou Y, Chang S. A visual weld edge recognition method based on light and shadow feature construction using directional lighting. J Manuf Process 2016;24:19–30. https://doi.org/10.1016/j.jmapro.2016.07.002.

[35] Iglesias C, Martínez J, Taboada J. Automated vision system for quality inspection of slate slabs. Comput Ind 2018;99:119–29. https://doi.org/10.1016/j.compind.2018.03.030.

[36] Wang J, Fu P, Gao RX. Machine vision intelligence for product defect inspection based on deep learning and Hough transform. J Manuf Syst 2019;51:52–60. https://doi.org/10.1016/j.jmsy.2019.03.002.

[37] Tsai DM, Lin CT. Fast normalized cross correlation for defect detection. Pattern Recognit Lett 2003;24:2625–31. https://doi.org/10.1016/S0167-8655(03)00106-5.

[38] Crispin AJ, Rankov V. Automated inspection of PCB components using a genetic algorithm template-matching approach. Int J Adv Manuf Technol 2007;35:293–300. https://doi.org/10.1007/s00170-006-0730-0.

[39] Kong H, Yang J, Chen Z. Accurate and Efficient Inspection of Speckle and Scratch Defects on Surfaces of Planar Products. IEEE Trans Ind Informatics 2017;13:1855–65. https://doi.org/10.1109/TII.2017.2668438.

[40] Masci J, Meier U, Ciresan D, Schmidhuber J, Fricout G. Steel defect classification with Max-Pooling Convolutional Neural Networks. Proc Int Jt Conf Neural Networks 2012:10–5. https://doi.org/10.1109/IJCNN.2012.6252468.

[41] He K, Gkioxari G, Dollar P, Girshick R. Mask R-CNN. Proc IEEE Int Conf Comput Vis 2017;2017-Octob:2980–8. https://doi.org/10.1109/ICCV.2017.322.

[42] Ferguson M, Ak R, Lee Y-TT, Law KH. Detection and Segmentation of Manufacturing Defects with Convolutional Neural Networks and Transfer Learning. Smart Sustain Manuf Syst 2018;2:20180033. https://doi.org/10.1520/ssms20180033.

[43] Zhang Q, Chang X, Bian SB. Vehicle-Damage-Detection Segmentation Algorithm Based on Improved Mask RCNN. IEEE Access 2020;8:6997–7004. https://doi.org/10.1109/ACCESS.2020.2964055.

[44] Wang H, Jiang Z, Zhang X, Wang Y, Wang Y. A fault feature characterization based method for remanufacturing process planning optimization. J Clean Prod 2017;161:708–19. https://doi.org/10.1016/j.jclepro.2017.05.178.

[45] Ren S, He K, Girshick R, Sun J. Faster R-CNN: Towards Real-Time Object Detection with Region Proposal Networks. IEEE Trans Pattern Anal Mach Intell 2017;39:1137–49. https://doi.org/10.1109/TPAMI.2016.2577031.

[46] Zhang Z. A Flexible New Technique for Camera Calibration. IEEE Trans Pattern Anal Mach Intell 2000;22:1330–4. https://doi.org/10.1109/34.888718.